



FOUNDATIONS
ADVANCES

Volume 74 (2018)

Supporting information for article:

Application of differential resonant high-energy x-ray diffraction to 3D structure studies of nanosized materials: A case study of Pt-Pd nanoalloy catalysts

Valeri Petkov, Sarvjit Shastri, Jong-Woo Kim, Shiyao Shan, Jin Luo, Jinfang Wu and Chuan-Jian Zhong

Supplementary Information:

Application of differential resonant high-energy x-ray diffraction to 3D structure studies of nanosized materials: A case study of Pt-Pd nanoalloy catalysts

Valeri Petkov¹, Sarvjit Shastri², Jong-Woo Kim², Shiyao Shan³, Jin Luo³, Jinfang Wu³ and Chuan-Jian Zhong³

¹Department of Physics, Central Michigan University, Mt. Pleasant, Michigan 48859, United States

²X-ray Science Division, Advanced Photon Source, Argonne National Laboratory, Argonne, Illinois 60439, United States

³Department of Chemistry, State University of New York at Binghamton, Binghamton, New York 13902, United States

i) 3D Periodic Crystallography Constrained Modeling

To ascertain the structure type of Pure, Pt, Pd and Pt_xPd_{100-x} alloy NPs (x=14, 36, 47, 64), the respective total atomic PDFs were approached with a simplistic model constrained to an fcc-type crystal structure. The model made sense because bulk Pt, Pd and Pt-Pd alloys are fcc-type crystals (Pearson, 1972). The initial model configurations featured atoms occupying identical sites in perfectly 3D periodic fcc-type lattices. The δ -functions-like peaks in the total atomic PDFs derived from the configurations were broadened by convolution with Gaussian functions as to mimic the thermal disorder and static structural distortions/relaxation typical for metallic NPs. The latter is documented by the considerable broadening of the first peak in the experimental PDF data for pure Pt NPs (see the inset in Figure 4b). At the same time the PDFs were multiplied by an artificial, rapidly decaying with real space distance function to mimic the finite size of the modeled NPs. Finally, the unit cell parameters of the model fcc-lattices were refined such that model-derived atomic PDFs approached the corresponding experimental PDFs as closely as possible. Computations were done with the help of the program PDFgui (Farrow *et al.*, 2007). Results from the computations, including the PDF-refined “fcc-lattice” parameters, are shown in Figures 5(a) and 5(b). Here it is to be underlined that “lattice parameters” for metallic NPs are not as well defined as a physical quantity as those for bulk metals and alloys. The reason is that the notion of “lattice parameters” implies the presence of perfectly 3D periodic lattices while metallic NPs are finite and possess a large surface area to volume ratio (see Figures 1 and 2). It is the surface of metallic NPs whereat the 3D periodicity of the atomic arrangement in the NPs is ultimately broken. Nevertheless, PDF data-derived “lattice parameters” for metallic NPs are useful merely because

they reflect the set interatomic distances characteristic for the studied NPs and so may be used as a “global descriptor” of those distances.

ii) Molecular Dynamics Simulations

Initial structure models for pure, Pt, Pd and Pt_xPd_{100-x} alloy NPs (x=14, 36, 47, 64) featured atomic configurations with the overall chemical composition, size (~5.3 nm), and shape (rounded polyhedra) of the modeled NPs. Atoms (~7000 in total) in the configurations were arranged in an fcc-like manner. The configurations were optimized in terms of energy, i.e. stabilized at atomic level, by classical Molecular Dynamics (MD) simulations based on the quantum-corrected Sutton-Chen (Q-SC) method (Sutton & Chen, 1990; Rafii-Tabar & Sulton, 1991, Kimura *et al.*, 1999). The optimization was performed under canonical NVT ensemble in the absence of periodic boundary conditions using the computer program DL-POLY (Smith *et al.*, 2002). Velocity Verlet algorithm with a time step of 2 fs was used. After an initial equilibration at 700 K for 20 ps, the model configurations were cooled down to room temperature (300 K) in steps of 50 K and equilibrated for further 100 ps.

The Q-SC method treats atomic pair interactions in metals and alloys as a sum of two constituents. One accounts for the repulsion between metal atom cores and the other accounts for the attractive force between metal atoms due to the sea of electrons around them. Accordingly, model's energy, U , appears as a sum of an atomic pair potential $V(r_{ij})$ term and a local electron density (ρ_i) term defined as follows:

$$U = \sum_i \left[\sum_{j \neq i} \frac{1}{2} \epsilon_{ij} V(r_{ij}) - c_i \epsilon_{ij} (\rho_i)^{\frac{1}{2}} \right] \quad (S1)$$

where

$$V(r_{ij}) = \left(\frac{a_{ij}}{r_{ij}} \right)^{n_{ij}} \text{ and } \rho_i = \sum_{j \neq i} \left(\frac{a_{ij}}{r_{ij}} \right)^{m_{ij}} \quad (S2)$$

Parameters $\epsilon_{ij}(\text{meV})$ and c_i are used to scale appropriately the interatomic repulsive $V(r_{ij})$ and attractive (ρ_i) interactions, respectively. Parameters m_{ii} and n_{ii} are positive integers such that $n_{ii} < m_{ii}$. The parameter a_{ij} is used to scale appropriately the distances r_{ij} between i and j type atoms in the structure models. Typically, a_{ij} is the fcc-lattice parameter for the respective bulk metal. Currently used Q-SC parameters for Pt and Pd are listed in Table S2 (Kimura *et al.*, 1999). At present, the Q-SC method derives the strength of interactions between unlike atoms, in particular the energy parameter ϵ_{ij} , as a geometric average of the respective ϵ_{ii} and ϵ_{jj} parameters, that is,

$\epsilon_{ij} = \sqrt{\epsilon_{ii}\epsilon_{jj}}$. The Q-SC parameter a_{ij} used to scale the distances between unlike atoms is also derived as a geometric average of the respective a_{ii} and a_{jj} parameters, that is, $a_{ij} = \sqrt{a_{ii}a_{jj}}$. The PDF-fit “lattice parameter” of Pt-Pd alloy NPs though evolves irregularly with the alloy’s composition (see Figure 5b), indicating that Pt and Pd atoms in NPs interact strongly and so are unlikely to form a homogenous solid solution (Gschneider & Vineyard, 1962; Denton & Ashcroft, 1991). The conjecture is supported by the evolution of the first peak in the Pt-Pt and Pd-Pd partial distribution functions shown in Figure 5d. Not surprisingly, atomic pair distances in the MD models based on the currently used Q-SC parameters did not match well the positions of the peaks in the experimental total and element-specific atomic PDFs, as exemplified in Figure S2. Hence, following a protocol described in (Prasai *et al.*, 2015) we adjusted the a_{ii} and ϵ_{ii} parameters for Pt and Pd by approximately 1.5 %. Most importantly, the parameter related to the strength of interaction between Pt and Pd (unlike) atoms, that is the ϵ_{ij} parameter, was derived as a harmonic ($\epsilon_{ij} = \frac{2\epsilon_{ii}\epsilon_{jj}}{\epsilon_{ii} + \epsilon_{jj}}$) instead of a geometric average of Pt-Pt (ϵ_{ii}) and Pd-Pd (ϵ_{jj}) interactions. MD models based on the so-modified Q-SC parameters matched the experimental PDF data better, as exemplified in Figure S3. The models were refined further by reverse Monte Carlo (RMC) computations as described below.

Reverse Monte Carlo Refinement of the MD models for pure Pt, Pd and Pt_xPd_{100-x} alloy NPs ($x=14, 36, 47, 64$)

Best MD models for pure Pt, Pd and Pt-Pd alloy NPs were refined further by RMC guided by the respective experimental total and element-specific PDF data sets (McGreevy & Pusztai, 1998). The refinement was necessary since actual metallic NPs exhibit significant static structural distortions/relaxation (e.g. see the inset in Figure 4b) and chemical patterns which may not be captured by MD alone, i.e. without experimental input. Total and element-specific PDFs are an excellent “experimental input” because, as demonstrated in Figures 4a, 4c, 5a, S4 and work of others (Jensen *et al.*, 2016; Kodama *et al.*, 2006; Olds *et al.*, 2015), they are experimental quantities sensitive not only to the atomic-scale structure but also to the size, shape and chemistry of metallic NPs. Details of the RMC refinement are described below:

1) The certainly large ensembles of metallic NPs studied by HE-XRD for the purposes of subsequent atomic PDF analysis, including the NP environment (e.g. porous carbon support, liquid

etc), constitute a continuous medium with a non-zero atomic number (electron) density, ρ_o , scattering x-ray photons into the detector. The density $\rho_o = \text{const} \neq 0$ appears in the traditional definition of the PDF $G(r) = 4\pi r(\rho(r) - \rho_o)$, where $\rho(r)$ is the local atomic number density (Klug & Alexander, 1974; Waseda, 1984; Egami, & Billinge, 2003). Typically, ρ_o is close to the average atomic number density of the studied NPs because the contribution of the NP environment to the scattered x-ray intensities is carefully corrected for in processing HE-XRD patterns into atomic PDFs. The above definition of $G(r)$ though is precise so long the studied ensembles of metallic NPs do not exhibit sizable large-scale (electron) density fluctuations that would result in a sizable (small-angle) scattering below q_{min} ($\sim 1 \text{ \AA}^{-1}$ in the present case) accessed in the HE-XRD experiments. If present and neglected, such density fluctuations would result in a small and featureless upshift of the physical oscillations of the experimental $G(r)$ data about zero (e.g. see Figures 1 and 3 in Cargill, 1971). The upshift would have little, if any, impact on the 3D structure models refined against the oscillations because the latter and not the former carry information about the atomic and chemical ordering in the studied NPs. Note that the physical oscillations of $G(r)$ are indeed sensitive to the NP size and shape and so can be used to differentiate between competing 3D structure for the NPs (e.g. see Figure S4). As generated, a finite size 3D model for metallic NPs though is not embedded in a medium with $\rho_o = \text{const} \neq 0$ density. Rather, its environment has zero density ($\rho_o=0$). Hence, $G(r)$ s computed from finite size 3D models of metallic NPs would not oscillate about “zero” as the experimental $G(r)$ s do (e.g. see Figure 2 in Olds *et al.*, 2015). Here we compute a smooth function, often referred to as a NP “shape” function, and combine it with the $G(r)$ s derived from the refined 3D models so that they oscillate about zero. Thus experimental and model-derived $G(r)$ s fall on a single curve, allowing a plausible 3D model to be refined against the experimental data in a straightforward manner. The computation of the “shape” function follows a protocol of the type described in ref. (Olds *et al.*, 2015).

2) It is well-known that atoms in metallic materials can experience both random atomic displacements, also known as (Debye-Waller type) thermal vibrations, and static displacements, i.e. relax. Hence, to decouple the latter from the former, peaks in the total and element-specific PDFs derived from the RMC-refined models were convoluted with a Gaussian broadening function,

$$F(r) = \frac{1}{\sigma_T \sqrt{2\pi}} * \exp\left(-\frac{r^2}{2\sigma_T^2}\right) \quad (\text{S3})$$

where r is the radial distance and σ_T is the thermal root-mean-square (rms) displacement of either Pt or Pd atoms at room temperature. The values of σ_T for Pt and Pd were taken from readily available databases with structure data for metals and alloys.

3) During the refinement, positions of atoms in the structure models were adjusted as to minimize the difference between the model-derived and experimental total and element-specific atomic PDFs (see the residual difference curves shown in Figure 7 in blue). The element-specific PDFs included differential PDFs (shown in Figure S1) and partial PDFs (shown in Figure 7, right).

4) Simultaneously, nearby Pt and Pd atoms were allowed to swap positions so long it helped minimize both the aforementioned difference and the energy of refined configuration (for the latter see step (7) below). Swapping was vital for achieving the good level of agreement between the RMC-fit and experimental atomic PDFs shown in Figure 7.

5) Furthermore, the RMC refinement was frequently switched between two modes of operation exemplified in Figure S5. That is, the atomic PDF data were represented either in terms of $G(r)$ or $r^*G(r)$ so that the atomic-level features of both the interior and the near-surface region of the modeled NPs are captured in due detail.

6) In addition, atoms in the refined 3D structures were required (i.e. restrained but not constrained) not to approach each other closer than pre-selected atomic pair distances, thereby taking into account the fact that metallic species in alloys may share valence electrons but remain distinct entities. Besides, atoms were required to pack as closely as possible, thereby taking into account the fcc-type character of the atomic arrangement in the modeled NPs.

7) Last but not least, the energy of the refined models was minimized further, i.e. beyond the level already achieved by MD, using pair-wise potentials taken from literature sources (Zhen & Davies; 1983).

Altogether, RMC refinements aimed at minimizing a residuals function χ^2 involving two major terms, χ_Ω^2 and χ_Θ^2 , defined as as follows (Petkov *et al.*, 2014).

$$\chi_\Omega^2 = \frac{\sum [G(tot)_i^{\text{exp}} - G(tot)_i^{\text{calc}}]^2}{\epsilon_{G(r)}^2} + \frac{\sum [G(Pt - Pt)_i^{\text{exp}} - G(Pt - Pt)_i^{\text{calc}}]^2}{\epsilon_{G(r)}^2} + \frac{\sum [G(Pd - Pd)_i^{\text{exp}} - G(Pd - Pd)_i^{\text{calc}}]^2}{\epsilon_{G(r)}^2} + \frac{\sum [CN_i^{\text{des}} - CN_i^{\text{calc}}]^2}{\epsilon_{CN}^2} + \frac{\sum [R_{ij}^{\text{des}} - R_{ij}^{\text{calc}}]^2}{\epsilon_{R_{ij}}^2} \quad (\text{S4})$$

$$\chi_\Theta^2 = \frac{\Delta U}{\epsilon_{\Delta U}^2} \quad (\text{S5}).$$

Here $G(tot)_i^{exp}$, $G(Pt-Pt)_i^{exp}$ and $G(Pd-Pd)_i^{exp}$ are experimental total and element-specific PDF data, and $G(tot)_i^{cal}$, $G(Pt-Pt)_i^{cal}$ and $G(Pd-Pd)_i^{cal}$ are model-derived total and element-specific PDF data, respectively. Furthermore, r is the radial distance, R_{ij}^{des} and R_{ij}^{cal} are preset plausible and model-derived ij atomic pair distances of closest approach, and CN_{ij}^{des} and CN_{ij}^{cal} are preset plausible and model-derived first coordination numbers (CNs) for an ij pair of atoms. The term ΔU reflects changes in model's energy as described by pair-wise potentials. The ε 's in the denominators of eqs. (S4) and (S5) are weighting factors allowing us to control the relative importance of the individual terms in the residuals function χ^2 being minimized. In the course of refinements the values of ε 's and rate of switching between the two modes of RMC operation exemplified in Figure S5 were changed several times to increase the chances of finding the global minimum of the residuals function χ^2 , instead of a local minimum. Note that using constraints, restraints, penalty functions etc. is a common practice in refining 3D structure models against diffraction data. Following that practice, we used them to guide the refinement and not to pre-determine its outcome. The RMC refinements were considered complete when no further minimization of the residuals function χ^2 was possible to be achieved. Computations were done with the help of a newer version of the program RMC++ allowing us to refine full-scale models for metallic NPs of any size and shape under non-periodic boundary conditions (Gereben & Petkov, 2013).

RMC-refined 3D models of pure Pt, Pd and Pt-Pd alloy NPs are shown in Figure 6. As can be seen in the Figures 7 and S1, total and element-specific PDFs derived from the models reproduce the respective experimental data sets in very good detail. The overall quality of the models was assessed by computing a goodness-of-RMC-fit indicator defined as

$$R_w = \left\{ \frac{\sum w_i (G_i^{exp.} - G_i^{calc.})^2}{\sum w_i (G_i^{exp.})^2} \right\}^{1/2} \quad (S6)$$

where $G^{exp.}$ and $G^{calc.}$ are experimental and RMC-fit (total or element-specific) PDFs, respectively, and w_i are weighting factors reflecting the experimental uncertainty of the individual data points. Here w_i were considered to be uniform which, as predicted by theory (Toby & Egami, 1992) and corroborated by experiment (Skinner *et al.*, 2013), is a reasonable approximation. The low R_w values (11-18 %) for the RMC-fits certify the high quality of the respective 3D atomic configurations. Here it is to be underlined that these configurations were i) generated taking into account data from complementarity ICP-OES, HR-TEM, HAADF-STEM and EDS experiments

and also findings of crystal-structure constrained modeling, ii) optimized in terms of energy by MD, iii) refined by RMC, iv) cross-checked by XPS and v) evaluated in terms of a goodness-of-RMC-fit indicator strictly following the successful practices of determining the 3D atomic structure of materials, in particular fine polycrystalline powders, by x-ray scattering techniques (Warren, 1969; David *et al.*, 2002). As such, within the limits of the experimental accuracy, the RMC refined 3D atomic configurations shown in Figure 6 can be considered as the most likely 3D atomic structures of the respective NPs.

iii) *X-ray photoelectron spectroscopy (XPS) studies on pure Pt and Pt_xPd_{100-x} alloy NPs (x=14, 36, 47, 64)*

XPS was used to evaluate the electronic properties and near surface composition of Pt-Pd alloy NPs studied here. Besides, it served as a litmus test of the accuracy of the findings of differential resonant XRD studies, in particular the evolution of Pt-Pt atomic pair correlations with the NP's composition. The measurements were done on Kratos AXIS Ultra DLD spectrometer using monochromatic Al source. The spectrometer was calibrated with respect to the Au 4f_{7/2} (84.0 eV) and Cu 2p_{3/2} (932.7 eV) lines. The pass energy was fixed at 20 eV for the detailed scans. The percentages of Pt and Pd species near the NP surface were determined by analyzing the areas of the respective XPS peaks. Typical XPS Pt 4f spectra for pure Pt and Pt-Pd alloy NPs are shown in Figure 10. Shifts in the binding energy of Pt species, as reflected by the shifts in the position Pt 4f_{7/2} lines, are also shown. The XPS determined near surface composition of Pt_xPd_{100-x} alloy NPs (x=14, 36, 47, 64) was found to be Pt_xPd_{100-x} (x=18, 32, 50, 61), respectively. Altogether, findings of ICP-OES, EDS and XPS experiments indicated that Pt and Pd atoms in Pt-Pd NPs studied here are well intermixed together (i.e. not-segregated). As discussed in the text, XPS data are also in line with the observed unusual shortening of Pt-Pt bonding distances in Pt-Pd alloy NPs.

iv) *Characterization of the activity of Pt_xPd_{100-x} alloy NPs (x=14, 47, 64) as catalysts for the ORR*

The catalytic activity of Pt_xPd_{100-x} alloy NPs (x=14, 47, 64) for the ORR was determined by cyclic voltammetry (CV) and rotating disk electrode (RDE) experiments. The experiments were performed on a three-electrode electrochemical cell using Pt wire as a counter electrode and Ag/AgCl (KCl sat.) as a reference electrode. Glassy carbon disk (geometric area, 0.196 cm²; polished with 0.05 μm Al₂O₃ powders) coated with a layer of carbon supported Pt-Pd alloy NPs

served as an working electrode. Data were collected with a computer controlled electrochemical analyzer (CHI600a, CH Instruments) at room temperature. The electrolytic solution (0.1 M HClO₄) was deaerated with N₂ before the CV measurements, or saturated with oxygen for the RDE measurements. Experimental data for the specific (SA) and mass activity (MA) of Pt-Pd alloy NPs for the ORR are shown in Figures 11(c) and 11(d), respectively. Also shown in the Figures are data for the ORR (SA and MA) activity of commercial (E-tek) nanosized Pt and Pd catalysts. More details of the CV and RDE measurements can be found in (Wu *et al.*, 2017).

iv) Assessing the surface electronic structure of pure Pt, Pd and Pt-Pd alloy NPs through DFT based on a revised version of the d-band center theory

Within the formalism of *d*-band center theory, the energy center of the *d*-electron band of an *i*-type surface transition metal atom, ε_{di} , varies linearly (negative slope) with the width of the *d*-band, w_{di} , as follows (Xin *et al.*, 2014; Hammer & Norskov, 2000; Jiang *et al.*, 2009; Kitchin *et al.*, 2004):

$$w_{di} = \sqrt{\frac{(1-3f_{di}+3f_{di}^2)}{3}} \left(\frac{1}{0.5-f_d} \right) \varepsilon_{di}, \quad (S7)$$

where f_{di} is the fractional filling of the *d*-band. Furthermore, within the same formalism, ε_{di} for an *i*-type surface transition metal atom can be derived as a sum of the matrix elements accounting for the bonding interactions between the atom and its immediate transition metal neighbors as follows:

$$w_{di} = \frac{\hbar^2}{m} \sum_{j=1}^{CN} \frac{[r_d^{(i)} r_d^{(j)}]^{3/2}}{d_{ij}^5}, \quad (S8)$$

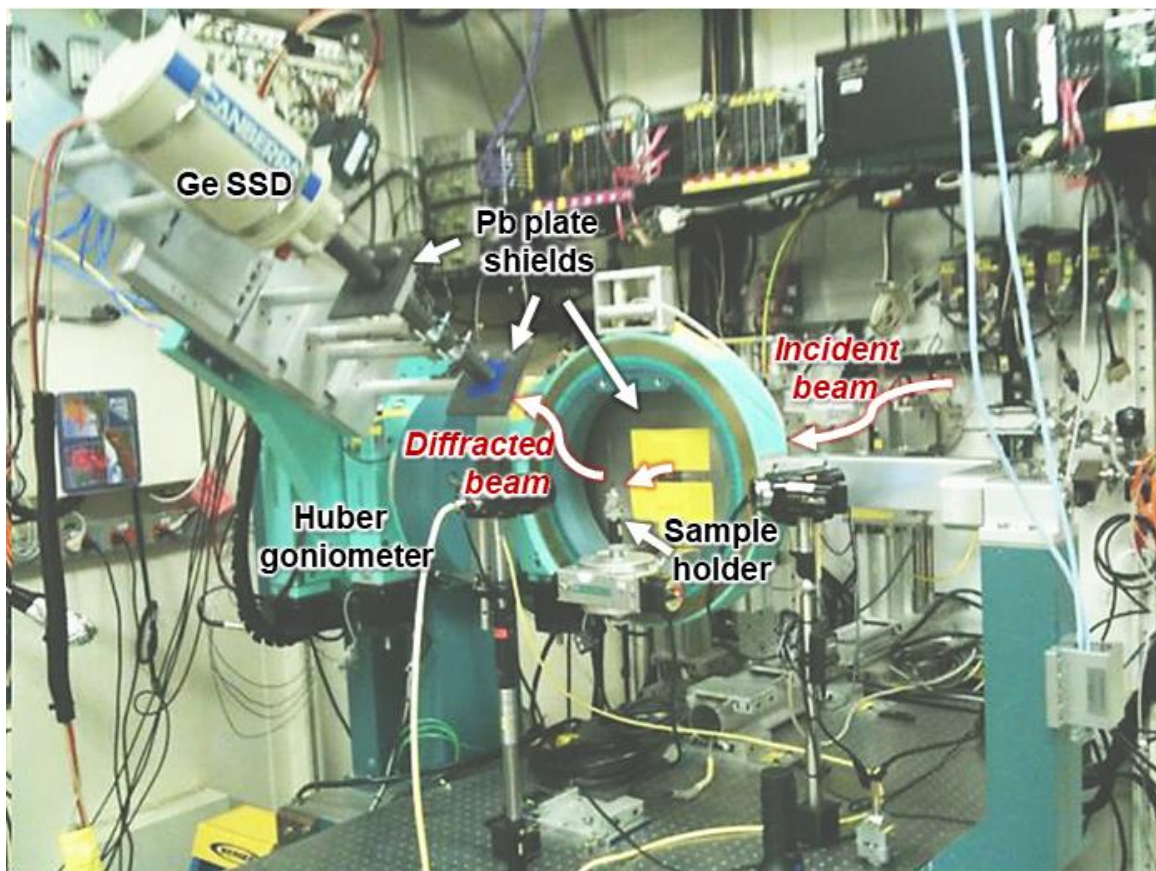
where m is the mass of the electron, $r_d^{(i)}$ and $r_d^{(j)}$ are, respectively, the characteristic size of nearby atoms of type *i* (e.g. Pt) and *j* (e.g. Pd) related to the spatial extent of their *d* orbitals, and d_{ij} is the actual *i-j* atomic pair distance. It is considered that i) surface metal-to-metal atom interactions, contributing to the so-called ligand effect, are taken into account through the respective $r_d^{(j)}$ terms and ii) surface structural distortions, contributing to the so-called strain effect, are taken into account through the d_{ij} terms. Furthermore, it is considered that the geometry of the NP surface is accounted for by the number of immediate neighbors, CN.

The w_{di} , and ε_d for each atom at the surface of pure Pt, Pd and Pt_xPd_{100-x} alloy NPs (x=14, 36, 47, 64) was computed from the respective 3D structures using *eqs.* (S7) and (S8) as parameterized

in ref. (Inoglu & Kitchin, 2010). The energy position of the upper end of the d -band, ε_w^d , for the atoms was computed as $\varepsilon_w^d = \varepsilon_{di} + w_{di/2}$ (Xin *et al.*, 2016). Color maps indicative of the catalytic activity of surface Pt and Pd atoms in the NPs, as measured by the respective ε_w^d values, are shown in Figure 11(b).

v) Experimental set-up for differential resonant high-energy x-ray diffraction studies

The experimental set-up used to conduct resonant HE-XRD studies at the K edge of Pt is shown in the photograph below. HE-XRD patterns were collected on a Huber goniometer in transmission geometry. Samples were sealed in thin-walled glass capillaries with a diameter of 1 mm. X-rays were delivered by a combination of a bent double-Laue monochromator and a four-crystal monochromator with an energy resolution $\Delta E \sim 8$ eV (Shastri *et al.*, 2002). Scattered x-rays intensities were collected with a solid-state Ge detector (Ge SSD).



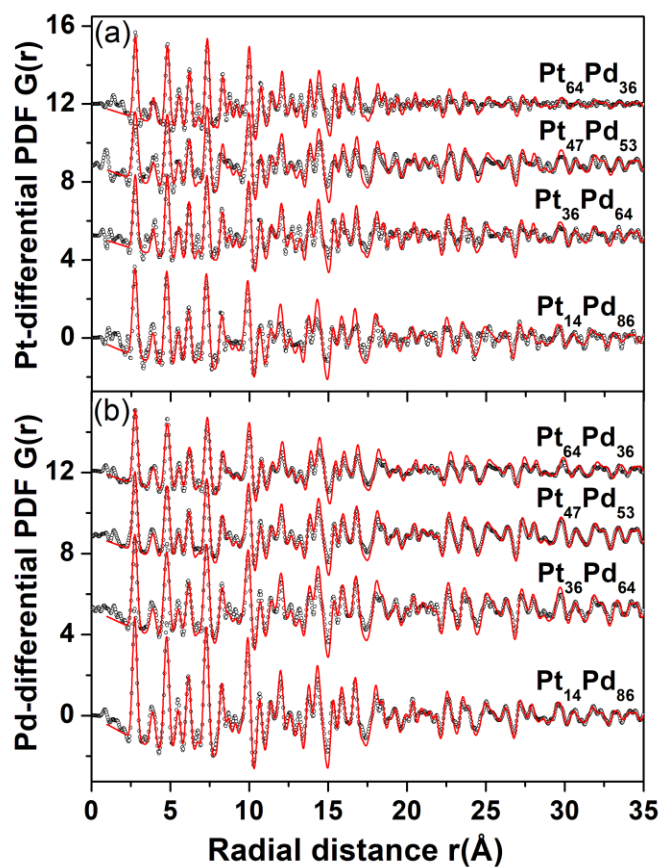


Figure S1. (a) RMC fits (red lines) to the experimental (symbols) Pt-differential PDFs for $\text{Pt}_x\text{Pd}_{100-x}$ alloy NPs ($x=14, 36, 47, 64$). (b) RMC fits (red lines) to the experimental (symbols) Pd-differential PDFs for the NPs. The fits reflect the respective 3D structures shown in Figure 6. The goodness-of-fit indicators R_w , defined by *eq. (S6)*, for the RMC fits are in the order of 12-18 %. Pt- and Pd-differential PDFs are obtained by differential resonant HE-XRD experiments at, respectively, the K edge of Pt and Pd, as described in the text.

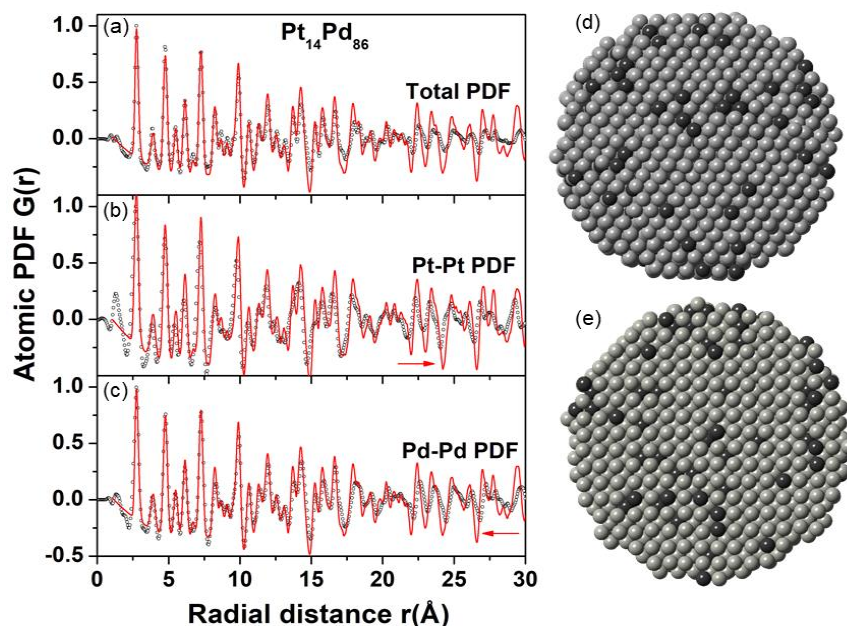


Figure S2. Comparison between experimental (symbols) total (a), Pt-Pt (b) and Pd-Pd (c) partial PDFs for $\text{Pt}_{14}\text{Pd}_{86}$ NPs and PDFs computed (red line) from the 3D model of the NPs shown on the right. The model (d) and a cross section of it (e) are optimized by MD based on the currently used Q-SC parameters (Table S2). Pt atoms are in black and Pd atoms are in gray. Experimental and computed atomic PDFs are systematically shifted with respect to each other (follow the arrows in (b) and (c)) because of the inadequacy of the currently used Q-SC parameters for Pt and Pd. Besides, the higher- r peaks in the model-derived PDFs appear much sharper in comparison with those in the experimental PDFs. That is because MD treats all atoms in structure models of metallic NPs in the same way while atoms in the interior and near surface region of actual metallic NPs do not necessarily have the same coordination environment.

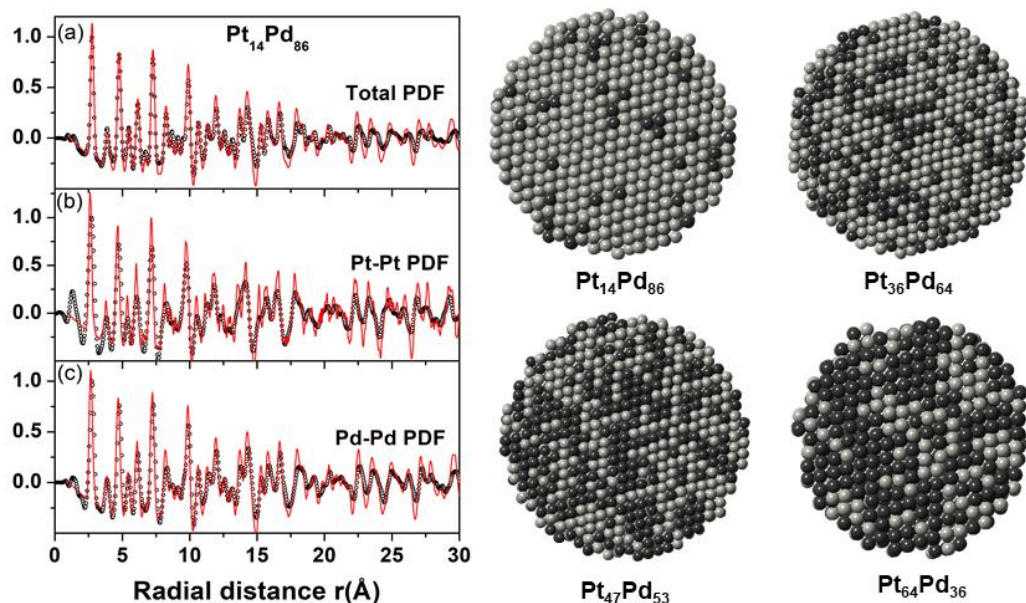


Figure S3. (*left*) Comparison between experimental (symbols) total (a), Pt-Pt (b) and Pd-Pd (c) partial PDFs for $\text{Pt}_{14}\text{Pd}_{86}$ NPs and PDFs computed (red line) from the 3D model of the NPs shown on the (right). The model is optimized by MD based on Q-SC parameters modified as described in Section ii) above. Pt atoms are in black and Pd atoms are in gray. The computed atomic PDFs approach the experimental data better in comparison with those shown in Figure S2. The observation indicates the usefulness of adjusting the parameters of the currently used potentials for modelling the 3D structure of nanosized materials, in particular metallic NPs. In general, the adjustment is necessary because the currently used potentials are calibrated against data for bulk metals and alloys (Prasai *et al.*, 2015). Yet, the longer-range atomic correlations in the improved MD model for $\text{Pt}_{14}\text{Pd}_{86}$ NPs appear stronger than those in the actual $\text{Pt}_{14}\text{Pd}_{86}$ NPs are (compare the higher- r peaks in the model-derived and experimental PDF data). This is one of the reasons for refining the model further by RMC. Also shown on the (*right*) are 3D models for $\text{Pt}_{36}\text{Pd}_{64}$, $\text{Pt}_{47}\text{Pd}_{53}$ and $\text{Pt}_{64}\text{Pd}_{36}$ alloy NPs. The models are optimized by MD based on Q-SC parameters modified as described in Section ii) above. The models were further refined by RMC as described in Section iii) above.

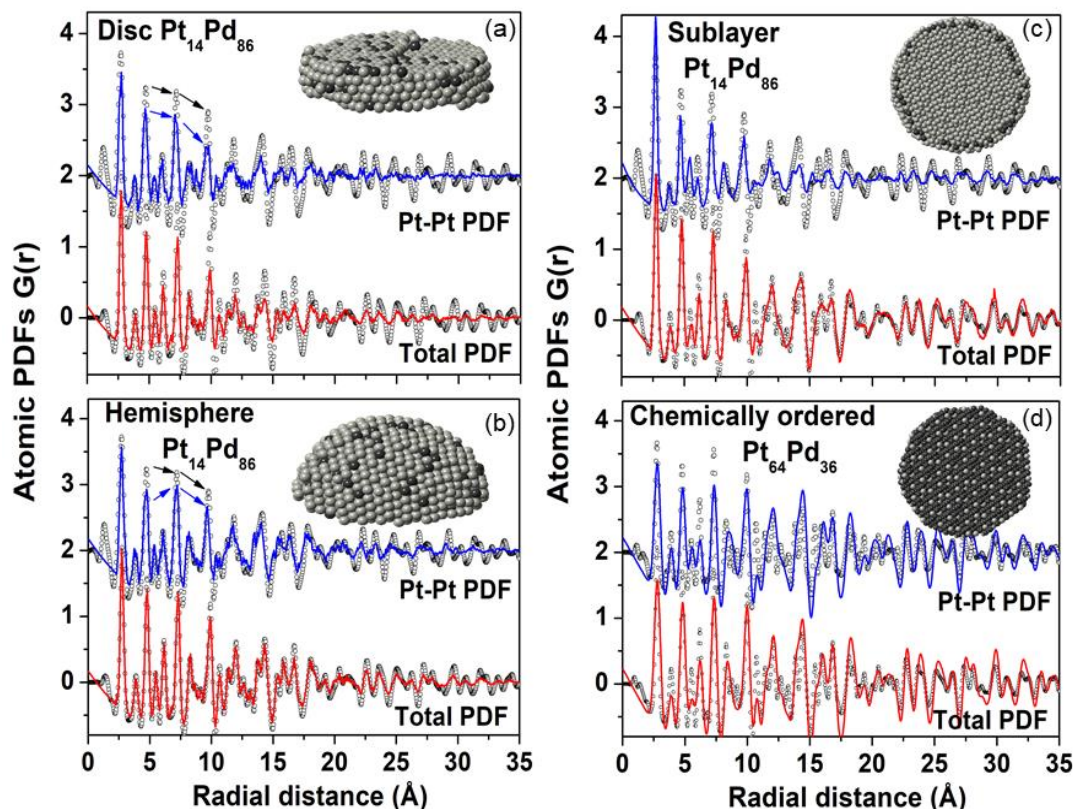


Figure S4. (a, b and c) Experimental (symbols) and computed (red line) total and Pt-Pt partial PDFs for $\text{Pt}_{14}\text{Pd}_{86}$ alloy NPs. (d) Experimental (symbols) and computed (red line) total and Pt-Pt partial PDFs for $\text{Pt}_{64}\text{Pd}_{36}$ alloy NPs. Computed PDFs in (a) are derived from a model featuring a disc with an average composition of $\text{Pt}_{14}\text{Pd}_{86}$ and diameter of approximately 5.3 nm. The model is shown in the upper right corner. Computed PDFs in (b) are derived from a model featuring a hemi-sphere with an average composition of $\text{Pt}_{14}\text{Pd}_{86}$ and diameter of approximately 5.3 nm. The model is shown in the upper right corner. The experimental and model-derived PDFs in (a) and (b) disagree in several important details (e.g. follow the arrows). The disagreement attests to the sensitivity of total and element-specific PDFs to the shape of metallic alloy NPs. Computed PDFs in (c) are derived from a model with the actual shape (rounded polyhedron), size (~ 5.3 nm) and overall chemical composition of $\text{Pt}_{14}\text{Pd}_{86}$ alloy NPs. The model is shown in the upper right corner. Pt atoms in the model though exclusively occupy its subsurface layer, which is at odds with the RMC-refined 3D structure for the NPs shown in Figure 6. The experimental and model-derived PDFs disagree. The disagreement attests to the sensitivity of total and element-specific atomic PDFs to the mutual distribution of distinct atomic species in metallic alloy NPs. (d) Experimental (symbols) and computed (red line) total and Pt-Pt partial PDFs for $\text{Pt}_{64}\text{Pd}_{36}$ alloy NPs. Computed PDFs are derived from a model with the actual shape (rounded polyhedron), size (~ 5.3 nm) and overall chemical composition of $\text{Pt}_{64}\text{Pd}_{36}$ alloy NPs. The model is shown in the upper right corner. Pt and Pd atoms in the model though are arranged in a completely chemically ordered pattern, which is at odds with the RMC-refined 3D structure for the NPs shown in Figure 6. The experimental and model-derived PDFs disagree. The disagreement attests to the sensitivity of total and element-specific atomic PDFs to the degree of chemical ordering in metallic alloy NPs. Pd and Pt atoms in all models shown here are in gray and black, respectively.

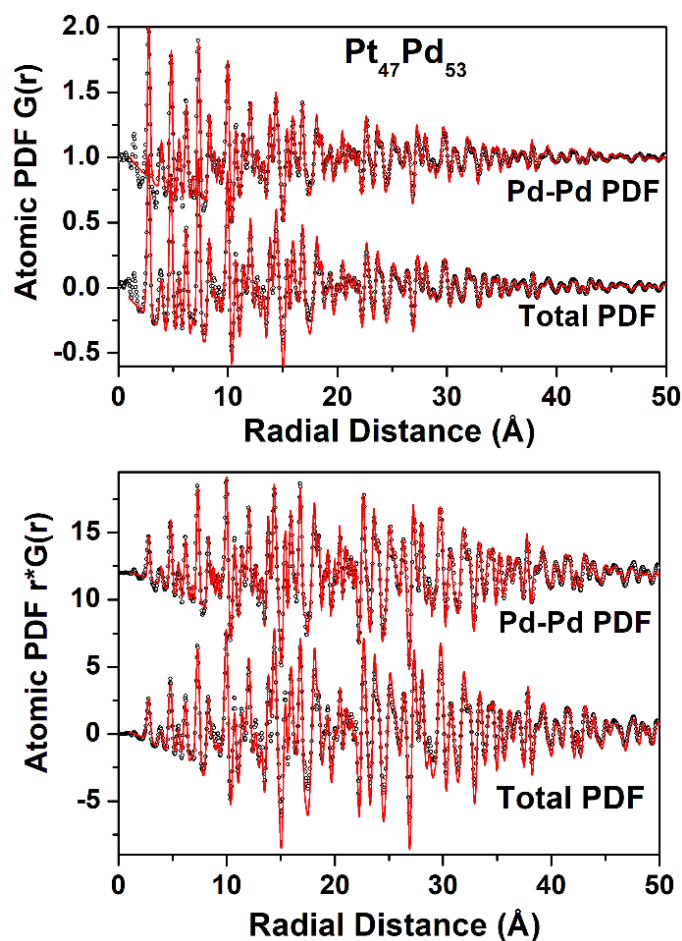


Figure S5. (*first row*) Experimental (symbols) and RMC-fit (red line) total and Pd-Pd partial PDFs $G(r)$ for $\text{Pt}_{47}\text{Pd}_{53}$ alloy NPs, where $G(r) = 4\pi r(\rho(r) - \rho_0)$. RMC-fits correspond to the 3D structure for the NPs shown in Figure 6. (*second row*) The same experimental (symbols) and RMC-fit (red line) data, this time represented as $r \cdot G(r)$, where r is the radial distance. Comparison between data sets in the (*first*) and (*second*) row shows that: i) RMC fits to experimental $G(r)$ s are largely sensitive to the immediate and medium-range correlations (relatively low- r PDF peaks) between atoms in the modeled NPs and ii) RMC fits to experimental $r \cdot G(r)$ s have an enhanced level of sensitivity to the immediate and longer-range correlations (higher- r PDF peaks) between atoms in the modeled NPs. Note that, as illustrated in Figure 4c, the longer-range correlations largely involve atoms near the NP surface. Alternating the RMC refinement between $G(r)$ and $r \cdot G(r)$ modes of fitting the experimental PDF data ensures that the resulting 3D structures describe well the atomic arrangement throughout the modeled NPs, including their near surface region.

Table S1. Weighting factors w_{ij} for $G_{Pt-Pt}(r)$, $G_{Pt-Pd}(r)$ and $G_{Pd-Pd}(r)$ partial PDFs for Pt_xPd_{100-x} alloy NPs ($x=0, 14, 36, 47, 64, 100$). Factors are defined in *eq.* (8). The contribution of distinct atomic pair correlations to the experimental PDF data is significant for each of the NPs.

Composition	w_{Pt-Pt}	$2 w_{Pt-Pd}$	w_{Pd-Pd}
Pure Pt	100 %		
Pt ₁₄ Pd ₈₆	6 %	34 %	60 %
Pt ₃₆ Pd ₆₄	24 %	50 %	26 %
Pt ₄₇ Pd ₅₃	36 %	48 %	16 %
Pt ₆₄ Pd ₃₆	55 %	49 %	7 %
Pure Pd			100 %

Table S2. Real $\Delta f'(E)$ and imaginary $\Delta f''(E)$ dispersion corrections to the scattering factors of Pt and Pd used in the present work.

Atomic species	$E=78.370$ keV	$E=78.070$ keV	$E=24.315$ keV	$E=24.015$ keV
Pt	$\Delta f'=-7.8; \Delta f''=0.6$ (*)	$\Delta f'=-4.1; \Delta f''=0.62$ (*)	$\Delta f'=0.3; \Delta f''=4.9$ (x)	$\Delta f'=0.3; \Delta f''=5.0$ (x)
Pd	$\Delta f'=0.32; \Delta f''=0.48$ (x)	$\Delta f'=0.33; \Delta f''=0.48$ (x)	$\Delta f'=-5.72; \Delta f''=0.54$ (*)	$\Delta f'=-2.7; \Delta f''=0.56$ (*)

(*) Values obtained by experiment described in the text

(x) Values taken from literature sources (Chantler, 1995)

Table S3. Currently used Q-SC parameters for Pt and Pd (Kimura *et al.*, 1999).

Note that the value of Q-SC parameter a_{ij} for a given atom and the size of that atom are directly related to each other since, for an fcc-type structure, atomic $size_{ij} = a_{ij} / \sqrt{2}$.

Metal	m_{ii}	n_{ii}	ε_{ii} (meV)	a_{ii} (Å)	c_i	$size_{ij}$ (Å)
Pt	7	11	9.7894	3.924	71.336	2.775
Pd	6	12	3.2864	3.891	148.20	2.755

SI References:

- Cargill, G. S. (1971). *J. Appl. Cryst.* **4**, 277-283.
- Chantler, C. T. (1995). *J. Phys. Chem. Ref. Data* **24**, 71-643.
- David, W. I. F., Shakland, K., McCusker, L. B. & Baerlocher, C. (2002). Oxford: Oxford University Press.
- Denton, A. R. & Ashcroft, N. W. (1991) *Phys. Rev. A* **43**, 3161-3163.
- Egami, T. & Billinge, S. J. L. (2003). *Underneath the Bragg Peaks: Structural Analysis of Complex Materials*. New York: Pergamon Press.
- Farrow, L., Juhas, P., J. Liu, J. W., Bryndin, D., Bozin, E., Bloch, J., Proffen, Th. & Billinge, S. J. L. (2007). *J. Phys.: Condens. Matter.* **19**, 335219.
- Gereben, O. & Petkov, V. (2013). *J. Phys.: Condens. Matter* **25**, 454211-9.
- Gschneider K. A. & Vineyard G. H. (1962). *J. Appl. Phys.* **33**, 3444-3450.
- Hammer, B. & Norskov, J. K. (2000). *Adv. in Catalysis* **45**, 71-129.
- Inoglu, N. & Kitchin, J. R. (2010). *Mol. Simul.* **36**, 633-638.
- Jensen, K. M.Ø., Juhas, P., Tofanelli, M. A., Heinecke, C. L., Vaughan, Ackerson G. C. J. & Billinge, S. J. L. (2016) *Nat. Comm.* **7**, 11859.
- Jiang, T., Mowbray, D. J., Dobrin, S., Falsig, H., Bligaard, T. & Norskov, J. K. (2009). *J. Phys. Chem.* **113**, 10548-10553.
- Kitchin, J. R.; Norskov, J. K.; Barteau, M. A.; Chen, J. G. (2004) *J. Chem. Phys.* **120**, 10240-10246.
- Kimura, Y., Qi, Y., Cagin, T. & Goddard, W. A. III (1999) *MRS Symp. Ser.* **554**, 43-48.
- Kodama, K., Iikubo, S., Taguchi, T. & Shamoto, S. (2006). *Acta Cryst. A* **62**, 444-453.
- Klug, P. K. & Alexander, L. E. (1974). *X-Ray Diffraction Procedures: For Polycrystalline and Amorphous Materials*. Wiley-INTERSCIENCE.
- McGreevy, R.L. & Pusztai, L. (1998). *Molec. Simul.* **1**, 359-367.
- Olds, D., Hsiu-Wen Wang, H.-W. & Page K. (2015). *J. Appl. Cryst.* **48**, 1651-1659.
- Pearson, W. B. (1972). *The crystal chemistry and physics of metals and alloys*. New York: Wiley-INTERSCIENCE.
- Petkov, V., Prasai, B., Ren, Y., Shan, S., Luo, J., Joseph, P., Zhong, C.-J. (2014). *Nanoscale* **6**, 10048-10061.
- Prasai, B., Wilson, A. R., Wiley, B. J., Ren, Y. & Petkov, V. (2015). *Nanoscale* **7**, 17902-17922.
- Rafii-Tabar, H. & Sulton, A. S. (1991). *Philos. Mag. Lett.* **63**, 217-224.
- Shastri, S. D., Fezzaa, K., Mashayekhi, A., Lee, W.-K., Fernandez, P. B. & Lee, P. L. (2002). *J. Synchrotron Rad.* **9**, 317-322.
- Skinner, L. B., Huang, C., Schlesinger, D., Petterson, L. G. M., Nillson, A. & Benmore, C. J. (2013). *J. Chem. Phys.* **138**, 074506-12.
- Smith, W., Yong, W. C. & Rodger P. M. (2002). *Molec. Simul.* **28**, 385-471.
- Sutton, A. P. & Chen J. (1990). *Philos. Mag. Lett.*, **61**, 139-146.
- Toby, B. H. & Egami, T. (1992). *Acta Cryst. A* **48**, 336-346.
- Warren, B. E. (1969). "X-ray Diffraction" Addison-Wesley.
- Waseda, Y. (1984). *Novel Applications of Anomalous (Resonance) X-Ray Scattering for Characterization of Disordered Materials*. Berlin: Springer.
- Wu, J., Shan, Sh., Cronk, H., Chang, F., Kareem, H., Zhao, Y., Luo, J., Petkov, P. & Zhong, Ch.-J. (2017). *J. Phys. Chem. C* **121**, 14128-14136.
- Xin, H., Vojvodic, A., Voss, J., Norskov J. K. & Abild-Pedersen, F. (2014). *Phys. Rev. B* **89**, 115114-5.
- Zhen, S. & Davies, G. J. (1983). *Phys. Stat. Sol.* **78a**, 595-605.